Biogenic synthesis of PdNCs embedded α-Fe₂O₃ microspheres using *Myrtus cumini L.* leaf extract and a Box-Behnken optimization of its Fenton-like catalytic activity

Venkatachalam C.D.[1*], Sengottian M.[1], Kandasamy S.[1] and Balakrishnan K.[2]

[1]Department of Chemical Engineering, Kongu Engineering College, Perundurai, Erode-638060, India

[2]Chemical Recovery Plant, Seshasayee Paper Boards Limited, Pallipalayam Erode-638007, India

Abstract

Microspheres (MSs) of paramagnetic iron oxide (α-Fe₂O₃) embedded with palladium nanocubes (PdNCs) were biosynthesized using *Myrtus cumini L.* leaf extract. The synthesized PdNCs embedded α-Fe₂O₃ microspheres were characterized using FTIR, XRD and SEM/EDX. The FTIR spectrum of the *Myrtus cumini L.* leaf extract confirmed the presence of phenol, ester and amine groups that were involved in the bio-reduction of PdCl₂ to PdNCs. SEM/EDX revealed that the PdNCs with size range of 15–250 nm were present on the surface of the synthesized microspheres. Box-Behnken Design (BBD) was employed for optimization of Methyl Orange (MO) decolorization using α-Fe₂O₃MSs and PdNCs embedded α-Fe₂O₃MSs at pH (1, 2 and 3), catalyst dosage (1, 3 and 5 g L⁻¹) and reaction irradiation time (30, 60 and 90 min). It was found that PdNCs embedded α-Fe₂O₃MSs had maximum decolorization of 96.56 % at pH 1.72, catalyst dosage 2.69 g L⁻¹ and irradiation time 68.34 min.

Keywords: Biogenic synthesis; *Myrtus cumini L.* leaf extract; PdNCs embedded α-Fe₂O₃ microspheres; Box-Behnken design; methyl orange.

1. Introduction

Iron oxide occurs in different forms such as wustite (FeO), FeO₂, hematite (Fe₂O₃), magnetite (Fe₃O₄), high pressure iron oxides (Fe₄O₅, Fe₅O₆, Fe₅O₇, Fe₂₅O₃₂, Fe₁₃O₁₉) and also as oxide–hydroxides like, goethite (α-FeOOH), akaganeite (β-FeOOH), lepidocrocite (γ-FeOOH) and ferrihyrite (FeOOH·4H₂O) that have extensive applications. Surface functionalized paramagnetic iron oxide particles are novel functional materials used in biotechnology and catalysis (Jamshaid *et al.*, 2016; Wang *et al.*, 2016; Zhou *et al.*, 2010). These particles have unique paramagnetic properties such as super-paramagnetic, high paramagnetic susceptibility, low Curie temperature, high coercivity, etc. Also they have a wide range of applications in magnetic fluids, data storage, clinic diagnosis, targeted drug delivery and catalysis (Sachdev *et al.*, 2017; Khani and Wipf, 2017; Patel *et al.*, 2008; Dias *et al.*, 2011).

Fe₂O₃ is inexpensive, abundant, very stable against photo-corrosion or chemical attack at neutral or basic pH with a band gap of 2.0 to 2.2 eV corresponding to the absorption of 564 to 620 nm light and also has strong adsorption capacity. By coating a fine layer of paramagnetic material like Pd, the catalytic activity of weak magnetic Fe₂O₃ particles can be enhanced and also Pd will act like a co-catalyst. Pd when coated on Fe/FeO core of size 300 Å showed maximum value of magnetization with 100 emu/g and coercivity greater than 700 Oe which makes it more suitable for easy recovery (Yiping *et al.*, 1994). Similar effect was seen in core-shell nanocluster catalysts where Pd coated on Cu showed a higher catalytic activity than noble metals like Au and Ag (Zhang *et al.*, 2019). Biogenic synthesis of metal and metal-oxide nanoparticles is an evolving method that would produce nanoparticles at ambient temperatures, neutral pH, low cost and in eco-friendly fashion (Parveen *et al.*, 2016). This approach does not require toxic chemicals and surfactants such as sodium borohydride (NaBH₄), sodium formaldehyde sulfoxylate (SFS) or sodium dodecyl sulfate (SDS) and polyvinyl pyrrolidone (PVP), synthetic thiols, amides, amines, carboxylic acid derivatives and phosphines as capping agents (Khanna *et al.*, 2009; Wang *et al.*, 2010; Newman and Blanchard, 2006). Plants naturally contain the functional characteristics of a reducing agent, thereby avoiding the application of these chemicals during nanoparticle synthesis. Biogenetic synthesis imparts steric stabilization of the particles against aggregation, increasing the surface area to volume ratio.

Palladium nanoparticles (PdNPs) were also synthesized superficially over reduced graphene oxide- carbon nanotube material sol-gel method using chemicals (NaBH₄ and Na₃C₆H₅O₇) (Sun *et al.*, 2013). In few other cases, carcinogenic chemicals like ethylene glycol, dimethyl

formamaide, dimethyl sulfide and ethanol were used, that has been avoided in this present study (Ugalde-Saldivar, 2011). There are many studies involving synthesis of iron oxide, palladium and other transition metal nanoparticles organically using vitamin B₂(Riboflavin) and biosynthesized using several leaf extracts namely *Sesbania grandiflora, Sargassum muticum, Glycine max* (L.) Merr, *Piper betle, Pistacia atlantica, Coffea arabica, Camellia sinensis, Cacumen Platycladi, Solanum trilobatum,* etc. (Nadagouda and Varma, 2008a; Rajendran and Sengodan, 2017; Mahdavi *et al.,* 2013; Petla *et al.,* 2012; Mallikarjuna *et al.,* 2013; Molaie *et al.,* 2012; Nadagouda and Varma, 2008b; Shahwan *et al.,* 2011; Zhan *et al.,* 2011; Ma *et al.,* 2014a, 2014b; Kanchana *et al.,* 2010). There are many applications of iron oxide and palladium nanoparticles reported in energy, environment, industry, healthcare, electronics, and food and agriculture fields (Ali *et al.,* 2016; Scheuermann *et al.,* 2009; Kidambi and Bruening, 2005).

Myrtus cumini L. tree is known to be native of the Indian sub-continent, and many others adjoining regions of South Asia. The fruit is commonly known as jambolan, black plum, Malabar plum, purple plum, Indian blackberry, and also as jamun (Malaya), java plum (Indonesia), wa (Thailand), va (Laos), pring bai (Cambodia) and damson plum (Jamaica) (URL: http://www.iucngisd.org/gisd/species.php?sc=505 (22.07.2018)). *Myrtus cumini L.* plant contains compounds like anthocyanins, glucosides, ellagic acids, iso-quercetin, other flavonols and flavonoids like kaemferol and myrecetin; with the leaves rich in compounds like glycosides, quercetin, myricetin, triterpenoids, esterase, galloyl carboxylase and tannin (Ayyanar and SubashBabu, 2012). *Myrtus cumini L.* leaf extract is utilized as a natural reducing and stabilizing agent during the synthesis of nanoparticles. Currently *Myrtus cumini L.* leaf, seed and bark extracts were used for synthesis of silver (Ag) and gold (Au) nanoparticles; mostly used in the biochemical applications (Kumar *et al.,* 2010; Raheman *et al.,* 2011; Logeswari *et al.,* 2015; Prasad *et al.,* 2012; Prasad and Swamy, 2013; Kumar and Yadav, 2012).

In the present study, an attempt has been made to utilize the phytochemical rich leaves of *Myrtus cumini L.* for the production of palladium nanoparticles coated paramagnetic iron oxide microspheres and its Fenton-like catalytic activity on decolorization of Methyl Orange (MO) dye was studied. Azo dyes are organic compounds having the functional group R–N5N–R' make up 60–70% of all dyes used to treat textiles, leather articles and some food materials, if absorbed by human body undergo reduction decomposition to form carcinogenic amines (Wakelyn, 2007). Orange G ($C_{16}H_{10}N_2Na_2O_7S_2$), Acid Orange 7 ($C_{16}H_{11}N_2NaO_4S$), Acid Orange 10 ($C_{16}H_{10}N_2Na_2O_7S_2$), Acid Yellow 17 ($C_{16}H_{10}Cl_2N_4Na_2O_7S_2$), Acid Red 1 ($C_{18}H_{13}N_3Na_2O_8S_2$), Acid Red 14 ($C_{20}H_{12}N_2Na_2O_7S_2$), Acid Black 1 ($C_{22}H_{14}N_6Na_2O_9S_2$) etc. are some of the commercially used azo dyes which has similar molecular structure as that of Methyl Orange ($C_{14}H_{14}N_3NaO_3S$) and it is taken as the simpler model compound for dye decolorization study (Shu and Huang, 1995; Tanaka *et al.,* 2000). Equation (1) gives the overall reaction involved during dye degradation.

$$C_{14}H_{14}N_3NaO_3S + 43H_2O_2 \rightarrow 14CO_2 + H_2SO_4 + NaNO_3 + 2HNO_3 + 48H_2O \quad (1)$$
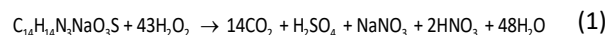
The degradation of Methyl Orange over PdNCs embedded α-Fe₂O₃ MSs occurs similar to that in the dielectric environment of a falling film reactor described in the literature (Wang *et al.,* 2017). The more the HO* ions, faster is the degradation of dye; in addition to that the excess H^+ and e^- starts another side reaction thereby breaking down the complex structure into simple compounds as shown in Equation 1. The use of iron oxide as Fenton catalysts has several advantages that include long catalyst lifetime, catalyst removal and reusability, operational pH range of 5 to 9 and insignificant effect of inorganic carbonates on the reactions (Nidheesh, 2015).

Response surface methodology (RSM) is a sophisticated statistical tool employed in effectively building mathematical models for processes involving multiple factors and also analyses their interactive effects on overall process (Soltani *et al.,* 2014). Box-Behnken design (BBD) is a quadratic factorial response surface methodology design that can be rotated along the center point of the of three cubes interlocked together within three (-1,0,+1) levels for each factor (Ferreira *et al.,* 2007). In this study, the synthesized particles by biogenic pathway were used as Fenton-like catalyst. The effects of process parameters such as pH, catalyst dosage and irradiation time on decolorization of MO were investigated and the optimal conditions to achieve maximum decolorization were determined using response surface methodology.

2. Materials and methods

2.1. Materials

Myrtus cumini L. plant was collected from K.K. Nagar, Erode and the plant specimen was identified and authenticated as *Syzygium cumini (L.)* Skells (=*Myrtus cumini* L.) Family: Myrtacea by Botanical Survey of India, Southern Regional Centre, Coimbatore, Tamil Nadu. The leaves of this plant were cleaned, dried in shade and crushed to fine powder and the underflow of Standard Sieve 25 (ASTM 30) of pore opening 0.6 mm was used for preparing the extract. 30 g of leaf powder was allowed to soak at room temperature in 500 mL of ethanol for 24 h in an orbital shaker at 150 rpm. Further, the leaf extract was filtered through Whatman filter paper No. 1 and stored under refrigeration below 4 °C for further experimental studies. FeCl₃·6H₂O (Nice Chemicals Pvt. Ltd., Kochi, India), Sodium acetate (Molychem, Mumbai), PdCl₂ (Indian Platinum Pvt. Ltd., MIDC, Vapi, India) and ethanol as solvent were used for the synthesis of PdNCs embedded α-Fe₂O₃MSs. Methyl Orange (Qualigens Fine Chemicals, Mumbai), H₂O₂ (Shivam Chemicals Reagent, Gurgon), H₂SO₄ (Molychem, Mumbai) and NaOH (Spectrum Reagents and Chemicals Pvt. Ltd, Cochin) were used for the Fenton catalytic studies. All chemicals used for the study were of analytical grade.

3. Experimental and characterization methods

3.1. Preparation of PdNCs embedded α-Fe₂O₃MSs

50 mL of 0.1 M $FeCl_3 \cdot 6H_2O$ solution (Figure 1a), 25 mL of freshly prepared *Myrtus cumini L.* leaf extract were mixed in conical flask (Figure 1b). 50 mL of 0.2 M sodium acetate solution was added drop by drop into the flask and stirred vigorously for 3 h at 70 °C using magnetic stirrer. The dark yellow solution turns to brown. One half of the solution was precipitated by adding 0.1 M NaOH by adjusting pH to slightly alkaline (8.0). The dark brown precipitate formed indicates the formation of α-Fe₂O₃MSs (Figure 1d) and it was separated by external magnetic field, filtered through Whatman filter paper No.1, washed twice using ethanol, centrifuged, dried overnight and stored. 20 mL of 0.1 M $PdCl_2$ solution was added in drops to the second half of the brown solution and stirred vigorously for 1 h at 60 °C using magnetic stirrer. The formation of PdNCs embedded α-Fe₂O₃MSs was marked by the appearance of intense black solution (Figure 1c) which was then precipitated by adding 0.1 M NaOH in drops till pH of the solution raises to 8.0. The final black precipitate of PdNCs embedded α-Fe₂O₃MSs (Figure 1e) obtained was isolated by applying an external magnetic field filtered, washed twice with ethanol, centrifuged, dried in a vacuum oven at 90 °C for 10 h and stored in an air tight container. The residual leaf extract solution (Figure 1f) after first filtration before washing was separately collected and stored under refrigeration below 4 °C for further testing.
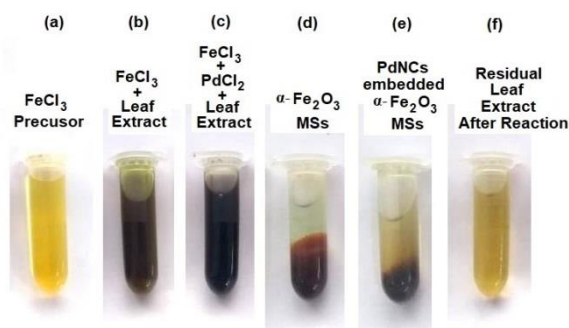
Figure 1. PdNCs embedded α-Fe₂O₃MSs synthesis

3.2. GC-MS analysis of Myrtus cumini L. leaf extract

Myrtus cumini L. ethanolic leaf extract was subjected to Gas Chromatography-Mass Spectrometer (GC-MS) analysis using Agilent 7890 with FID detector for GC and Jeol AccuTOF GCV for MS to find the phytochemicals from C1 to C20 that were responsible for bio-reduction and formation of nanoparticles. GC-MS is equipped with glass column of 0.53 mm internal diameter, 105 m length, and 0.25 μm film thickness. The sample size of 2 μL was injected through the injector with helium as carrier gas. The MS was taken at 70 eV of ionization energy. The carrier gas column flow and purge flow were fixed to 1 mL min⁻¹ and 5 mL min⁻¹ respectively with 50 °C as the initial temperature of the oven and a ramp of 22 min to 280 °C

and held for 35 min. The mass range was fixed from 45 to 300 amu, scan interval of 0.50 s, 260 °C with a split ratio of 10:0. Total running time of GC-MS was 65 min. The relative % amount of each component was expressed as a percentage with peak area normalization.

3.3. UV-Vis spectra analysis

The UV-Vis spectral analysis was done for the FeCl₃ precursor (0.1 M $FeCl_3 \cdot 6H_2O$ solution) and *Myrtus cumini* L. ethanolic leaf extract using Systronics UV-Vis Spectrophotometer 119 for spectral range between 200 to 800 nm. Both the dark yellow and brown solution formed during α-Fe₂O₃MSs synthesis was subjected to UV-Vis spectral analysis.

3.4. Fourier transform infrared (FT-IR) spectroscopy

FT-IR analysis was carried out for *Myrtus cumini* L. leaf powder and the PdNCs embedded α-Fe₂O₃MSs using Thermo Fisher Nicolet 6700 FT-IR spectrophotometer. 0.25 g of the leaf powder or the catalyst was mixed with 2.5 g of potassium bromide (KBr) and grounded thoroughly in a mortar with the pestle. The fine grounded powder was pressed at 5000-10000 psi into a pellet. The pellet was placed in the FT-IR sample holder and pressed using the metallic disc. FTIR analysis were also carried out for the leaf extract with 0.1 M $FeCl_3 \cdot 6H_2O$ solution and the residual leaf extract solution after precipitation of α-Fe₂O₃MSs by pH adjustment using Bruker 3000 Hyperion Microscope with Vertex 80 FTIR System under Single point detector of range 4000-450 cm⁻¹. IR was turned ON and once the device was ready with baseline correction, the sample tested for % Transmittance. The graph was plotted with the prominent peaks which were already selected and the result was provided with minimum disturbance by noise correction.

3.5. X-ray diffraction (XRD) analysis

The synthesized uncoated α-Fe₂O₃MSs and PdNCs embedded α-Fe₂O₃MSs were characterized using XRD. A Rigaku Ultima IV X-Ray Diffractometer instrument was used for the XRD analysis. The source of Cu Kα radiation (λ = 1.54 Å) with rated voltage and current 40 kV/40 mA was utilized. Both the sample were scanned within the 2θ range of 20–70° and to reduce the NaCl formed during the synthesis process, the samples were repeatedly washed with ethanol prior to XRD analysis.

3.6. SEM and EDS analysis

SEM and EDS analysis were carried out on uncoated α-Fe₂O₃MSs and PdNCs embedded α-Fe₂O₃MSs using a JEOL-JSM 6390 type Scanning Electron Microscope with INCA PENTA FET X instrument. The Pd uncoated and coated Fe₂O₃MSs powders were sprinkled onto black adhesive carbon tapes and fixed on metallic disks with in the vacuum chamber. Then the electron beams were focused onto the powder where the secondary electron, backscatter and X-ray were captured using a specialized detector that processes the signals into usable images and elemental contents.

3.7. Fenton-like catalytic activity of α-Fe₂O₃ MSs and PdNCs embedded α-Fe₂O₃ MSs

The decolorization of MO at initial concentration of 20 mg L^{-1}, temperature 50 °C and H_2O_2 concentration of 29.07 mM was carried out with pH (1, 2 and 3), catalyst dosage (1, 3 and 5 g L^{-1}) and reaction irradiation time (30, 60 and 90 min). 100 mL of 20 mg L^{-1} MO solution with required amount of α-Fe₂O₃ MSs and PdNCs embedded α-Fe₂O₃ MSs (g L^{-1}) and H_2O_2 (mM) were taken in a beaker. The initial pH of their action system was adjusted by addition of H_2SO_4. After sealing, the reaction solution was stirred by temperature controlled magnetic stirrer under the UV light source. The glass reactor was covered by aluminum foil for effective UV irradiation. The solution was clarified using Remi Centrifuge, India at the predetermined irradiation time. The aqueous phase was filtered and subjected to absorbance test and the decolorization rate (R_D) in terms of degree of color removal at the maximum absorbance 482 nm was calculated using the Equation (2).

$$R_D = \frac{A_o - A_t}{A_t} \times 100\% \qquad (2)$$

where A_o is the initial absorbance of MO and A_t is the absorbance at irradiation time 't'.

3.8. Box-Behnken design (BBD) optimization

Multiple regression analysis is a method to solve multivariable equation simultaneously and Response surface methodology (RSM) is one of the empirical statistical modeling techniques used most often now-a-days for optimizing a complex processes. RSM that reduces the experimental runs required was employed here to optimize the effect of independent process parameters such as pH, catalyst dosage and irradiation time on the decolorization of MO. The experiments were based on 2³ factorial BBD design having three factors with each independent variable coded at three levels +1, 0 and -1 correspond to the highest, middle and lowest level (Table 1). Coding of the variables was done using the Equation (3).

$$x_i = \frac{X_i - X_m}{\Delta X_i} \qquad (3)$$

where x_i is the dimensionless value of the independent variable, X_i is the real value of the independent variable, X_m is the real value of the independent variable at the midpoint and ΔX_i is the step change of the real value corresponding to a variation of a unit for the dimensional value of the variable i = 1,2,3,…k.

Table 1. Box-Behnken Design with independent variables and their levels

Variables, unit	Factors	Levels		
	X	-1	0	+1
pH	X₁	1	2	3
Catalyst Dosage (g L^{-1})	X₂	1	3	5
Irradiation time (min)	X₃	30	60	90

The total number of experimental runs (N) for BBD was calculated using the following Equation (4).

$$N = K^2 + K + C_p \qquad (4)$$

where K is number of factors and C_p is the number of central points. For normal three levels factorial design the number of runs will be 3³ i.e. 27. BBD eliminates the complex intermediate point responses and finally results with 17 runs for each catalyst with 5 central points (Maran *et al.*, 2015).

The response surface of the decolorization considering all linear, square and interaction terms using the second order polynomial equation is given by Equation (5).

$$Y = \beta_0 + \sum_{k=1}^{q} \beta_k x_{ki} + \sum_{k=1}^{q} \beta_{kk} x_{ki}^2 + \sum_{k=1}^{q-1} \sum_{l=k+1}^{q} \beta_{kl} x_{ki} x_{li} + \varepsilon_i \qquad (5)$$

where Y is the response for decolorization of MO; β_0 is the intercept coefficient; β_k, β_{kk} and β_{kl} are interaction coefficients of linear, quadratic and second order terms of model respectively; x_{ki} and x_{li} are process variables (k and l range from 1 to q); q is the number of independent parameters and ε_i is the error (Maran and Manikandan, 2012; Thirugnanasambandham *et al.*, 2014). The final equation for three independent parameters (q) with the error term is given by Equation (6).

$$Y = \beta_0 + \beta_1 x_1 + \beta_2 x_2 + \beta_3 x_3 + \beta_{11} x_1^2 + \beta_{22} x_2^2 + \beta_{33} x_3^2 + \beta_{12} x_1 x_2 \\ + \beta_{13} x_1 x_3 + \beta_{23} x_2 x_3 + \varepsilon_i \qquad (6)$$

Although the factors like temperature, H_2O_2 concentration and initial concentration of MO can be varied, but they were kept constant. The higher temperatures provide faster dye degradation accelerated the rate of HO* formation in a heterogeneous environment and it provides high energy for the reactant molecules to overcome the reaction activation energy barrier (Feng *et al.*, 2004). Ghorbanloo *et al.* (2015) investigated the effect of temperature on dye degradation and reported that the degradation followed a pseudo-first-order rate kinetics with rate constant k values increasing as the reaction temperatures were increased, which led to select 50 °C as an moderate temperature (Ghorbanloo *et al.*, 2015). Higher dosage of H_2O_2 causes decrease in the degradation efficiency of MO, which was mainly caused by the scavenging effect of excessive H_2O_2 to HO* therefore, a suitable H_2O_2 concentration of 29.07 mM was selected (Youssef *et al.*, 2016).

3.9. Statistical analysis

Multiple regression analysis and Analysis of Variance (ANOVA) with Pareto data were conducted to fit the mathematical model obtained using statistical tool Design Expert 8.0.7.1 (Stat Ease Inc., Minneapolis, USA). ANOVA is an exploratory statistical tool that analyzes the difference among group means and subdivides the total variation in a set of data into component parts associated with different sources of variation for the purpose of testing hypotheses on the selected parameters of the model (Kubiak and Benbow, 2009). The significance of regression model was evaluated using F-test and a quadratic model including linear, squared and interaction terms were used to state the model (Harrell, 2015). Significant terms in the mathematical model for each response were found by ANOVA and its adequacies were

checked in terms of the regression coefficient values of R^2, adjusted R^2 and prediction error sum of squares (PRESS). The regression coefficients data generated from the statistical calculation were used to plot response surfaces and contour plots.

3.10. Verification of predicted optimized conditions

Optimal conditions for the photocatalytic decolorization of MO using α-Fe$_2$O$_3$MSs and PdNCs embedded α-Fe$_2$O$_3$MSs that depends on pH, catalyst dosage and irradiation time were obtained using Derringer's desired function methodology. The experiments were carried out and the percentage decolorization of MO was determined

under the optimal conditions. The experimental values were compared with the predicted values of the developed model to find out its accuracy and suitability.

4. Results and discussion

4.1. GC-MS analysis of Myrtus cumini L. leaf extract

Table 2 shows the bio active components present in the *Myrtus cumini L.* ethanolic leaf extract that are responsible for the formation of α-Fe$_2$O$_3$ MSs and PdNCs from their respective precursors. The GC-MS analysis clearly denotes the abundance of hydroxyl and carboxylic groups that act as the reducing agent.

Table 2. GC-MS peaks and components in *Myrtus cumini L*. leaf extract

| Rt Time	Area %	Molecular Formula	Avg Mass	IUPAC Name
1.834	54.34	$C_4H_{10}O_2$	90.121 Da	2-Propanol, 1-methoxy-
2.438	1.11	C_2H_6O	46.068 Da	Ethanol
2.649	0.71	CH_2O_2	46.025 Da	Formic acid
2.821	3.08	$C_2H_7NO_2$	77.082 Da	Ammonium acetate
3.445	4.14	$C_3H_8O_3$	92.094 Da	Glycerin
3.923	2.28	C_3H_7NO	73.094 Da	Formamide, N,N-dimethyl-
9.41	3.59	$C_6H_5NO_2$	123.109 Da	Benzene, nitro-
10.692	0.63	$C_9H_{14}O$	138.207 Da	Bicyclo[3.1.1]heptan-2-one, 6,6-dimethyl-, (1R)-
10.774	1.49	$C_{10}H_{16}O$	152.233 Da	Bicyclo[3.1.1]heptan-3-ol, 6,6-dimethyl-2-methylene-, [1S-(1.alpha.,3.alpha.,5.alpha.)]-
11.227	0.66	$C_{10}H_{14}O$	150.218 Da	Pinocarvone
12.025	1.59	$C_{10}H_{14}O$	150.218 Da	(1R)-(-)-Myrtenal
12.104	1.02	$C_{10}H_{16}O$	152.233 Da	Bicyclo[3.1.1]hept-2-ene-2-methanol, 6,6-dimethyl-
12.376	1.38	$C_{10}H_{14}O$	150.218 Da	Bicyclo[3.1.1]hept-3-en-2-one, 4,6,6-trimethyl-, (1S)-
18.661	1.25	$C_{15}H_{24}$	204.351 Da	Alloaromadendrene
19.483	0.72	$C_{15}H_{24}$	204.351 Da	Naphthalene, 1,2,4a,5,6,8a-hexahydro-4,7-dimethyl-1-(1-methylethyl)-
19.818	2.11	$C_{15}H_{24}$	204.351 Da	γ-Muurolene
19.913	2.30	$C_{15}H_{24}$	204.351 Da	Naphthalene, 1,2,3,5,6,8a-hexahydro-4,7-dimethyl-1-(1-methylethyl)-, (1S-cis)-
21.547	0.69	$C_{16}H_{34}$	226.441 Da	Hexadecane
21.901	0.66	$C_{15}H_{24}O$	220.350 Da	12-Oxabicyclo[9.1.0]dodeca-3,7-diene, 1,5,5,8-tetramethyl-, [1R-(1R*,3E,7E,11R*)]-
22.518	3.42	$C_{15}H_{26}O$	222.366 Da	τ-Cadinol
22.794	4.08	$C_{15}H_{26}O$	222.366 Da	α-Cadinol
24.319	3.83	$C_{15}H_{26}O_2$	238.366 Da	7-Acetyl-2-hydroxy-2-methyl-5-isopropyl bicyclo[4.3.0]nonane
28.264	1.97	$C_{15}H_{30}O_2$	242.398 Da	Pentadecanoic acid
30.621	1.84	$C_{20}H_{40}O$	296.531 Da	Phytol
31.131	1.11	$C_{14}H_{26}O$	210.356 Da	7-Tetradecenal, (Z)-

4.2. UV-Vis spectra analysis
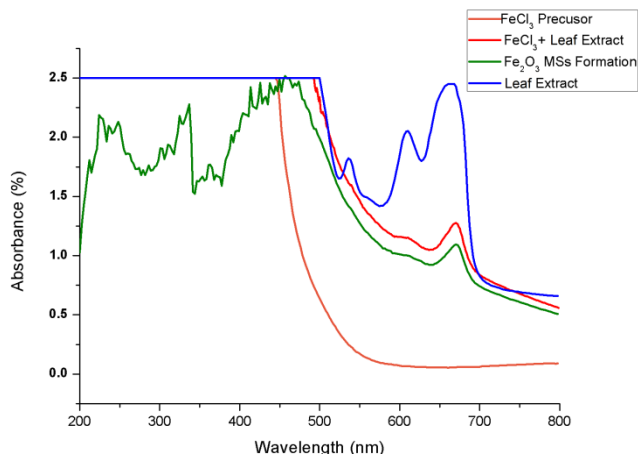
Figure 2. UV absorption spectra

Figure 2 shows the UV-Vis spectra of $FeCl_3$ precursor, *Myrtus cumini L.* leaf extract and indicates that the absorbance of $FeCl_3$ precursor solution dropped at 440 nm during the addition of leaf extract pertaining to the reduction reaction involving formation of α-Fe_2O_3 MSs. The resulting brown solution produced peaks at 340 and 440 nm which indicated fingerprints of Fe_2O_3.

4.3. Fourier transform infrared (FT-IR) spectroscopy

The synthesized α-Fe_2O_3MSs particles from *Myrtus cumini L.* leaf extract were analyzed by FT-IR spectroscopy to find out the functional groups present in it. The FT-IR spectrum of Fe_2O_3MSs in Figure 3 displays several bands at 467.23, 540.33, 1620.19 and 3416.62 cm⁻¹. Strong peak observed at the frequency of 467.23 and 540.33 cm⁻¹ was due to Fe-O-Fe stretching vibration corresponding to the α-Fe_2O_3MSs. Medium peak at 1620.19 cm⁻¹ indicates the O-H bending vibrations and weak peaks at 1402.05, 1541.87 cm⁻¹ and 1743.41 cm⁻¹ assigned to symmetric and asymmetric O5C5O stretching vibration. The broad peak at 3416.62 cm⁻¹ indicates the O-H stretching bond vibration due to the water adsorption on the surface of α-Fe_2O_3MSs.
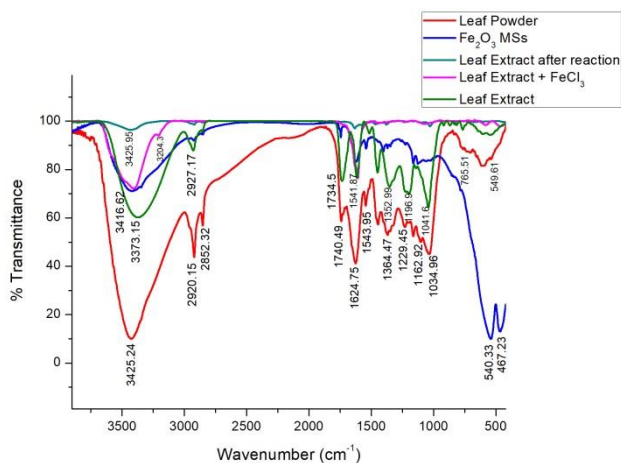

Figure 3. FTIR spectra

The FT-IR spectrum of *Myrtus cumini* L. leaf powder in Figure 3 displays several bands. The broad N-H wag between 910-665 cm⁻¹ correspond to the presence of primary and secondary amines. The weak peaks observed at 1034.96, 1162.92, 1229.45 and 1624.75 cm⁻¹ was due to aliphatic amines while the medium peaks at frequencies 1368.47 and 1543.95 cm⁻¹ shows the presence of nitro compounds. The stretch at peaks 1740.49, 2852.32 cm⁻¹ and 2920.15 cm⁻¹ corresponding to C5O and H-C5O confirms the presence of ester, aldehydes and saturated aliphatic compound. The broad and sharp peak at 3425.25 cm⁻¹ corresponds to the rich phenolic content in the leaf extract. These compounds act as the reducing agent in the formation of Fe_2O_3MSs and PdNCs. The FT-IR spectrum of the leaf extract with the precursor before and after the reaction in Figure 3 shows that several bands 1734.45, 2927.17 cm⁻¹ corresponding to the ester, aldehyde groups has diminished. The peaks 1352.99, 1196.9 and 1041.6 cm⁻¹ assigned to symmetric O5C5O stretching vibration diminished instantly, leaving the asymmetric carboxylic acids as such corresponding to peak at 1541.87 cm⁻¹. Even this diminished after the addition of 0.1 M NaOH for pH adjustment. This shows the strong interaction between the bioactive components and the $FeCl_3$ precursor in the synthesis of α-Fe_2O_3MSs. The peaks 3373.15 and 3425.95 cm⁻¹ corresponding to O-H stretching bond vibration indicates the presence of residual polyphenolic groups and water present after the completion of reaction.

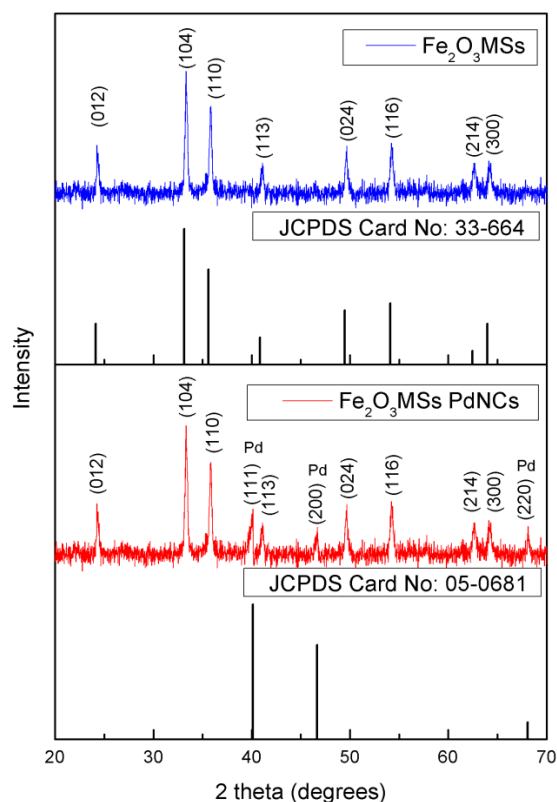## 4.4. X-ray diffraction (XRD) analysis

Figure 4. XRD spectra

Figure 4 illustrates the XRD patterns of biogenically synthesized α-Fe_2O_3 MSs and PdNCs embedded α-Fe_2O_3 MSs respectively. It has been found that both the particles are polycrystalline linked by matrixes of organic compounds and the peaks of the patterns are indexed in accordance with the XRD Spectra of α-Fe_2O_3 given in the NBS (National Bureau of Standards) Monographs 25 Section 18 (or JCPDS Card No: 33-664) and pattern of PdNCs in the NBS Monographs 25 Section 1 (or JCPDS Card No: 05-0681) of U.S. Department of Commerce.

It was also found that the intensities of the Bragg peaks were intense and narrow for the orientation of the peaks (104), (110), (024) and (116) and (111), (200) and (220) that are in accordance with the standard α-Fe_2O_3 and PdNCs respectively, thus confirming better crystallinity. The angle of diffraction of X-rays 2θ, the distance between atomic layer in the crystal d and the intensities of the peaks in the XRD pattern of the samples and the standards are given in Table 3. The crystallite size of α-$Fe_2O_3$was calculated using peak broadening profile of (104) peak at $33.33°$ and Debey-Sherrer's formula as shown below in Equation (7).

$$d = \frac{k\lambda}{\beta\cos\theta} \qquad (7)$$

where d is the crystallite size, k is shape factor (0.9), λ is wavelength of X-ray (1.5418 Å), β the full-width at half-maximum (FWHM) of a peak corresponding to the diffraction angle ϑ. The crystallite size was found to be 5 nm.

Table 3. Structural parameters of standards and PdNCs embedded α-Fe_2O_3 MSs

h l k	JCPDS #33-664 (α-Fe_2O_3)			PdNCs embedded α-Fe_2O_3 MSs			
	2θ degree	d nm	Intensity (%)	2θ degree	Intensity (%)	β	d nm
0 1 2	24.14	3.684	30	24.28	27	0.4157	3.662
1 0 4	33.15	2.700	100	33.33	100	0.6183	2.686
1 1 0	35.61	2.519	70	35.81	87	0.6828	2.506
1 1 3	40.86	2.207	20	41.10	20	0.8389	2.195
0 2 4	49.48	1.841	40	49.68	35	1.1693	1.834
1 1 6	54.09	1.694	45	54.22	43	1.4043	1.690
2 1 4	62.45	1.599	10	62.56	36	2.0291	1.484
3 0 0	63.99	1.486	30	64.10	28	2.1879	1.452
JCPDS #05-0681 (Pd)							
1 1 1	40.11	2.245	100	40.14	75	0.8085	2.245
2 0 0	46.66	1.944	42	46.68	31	1.0404	1.944
2 2 0	68.08	1.375	25	68.12	18	2.7080	1.375

The crystallite size d from the JCPDS Cards and d calculated from Equation (7) as given in Table 3 were compared to obtain the average error to be 1.115 %. This shows maximum correlation between the standard crystallite structures and structure of the synthesized PdNCs embedded α-Fe_2O_3 MSs.

4.5. SEM and EDS analysis

SEM analysis was carried out to find surface morphology of α-Fe_2O_3MSs and PdNCs embedded α-Fe_2O_3MSs at different magnifications x7500, x1000, x20000 and x30000. Figure 5a the micrograph of α-Fe_2O_3MSs showed fusion of smaller spheres into larger particles and FT-IR results confirmed the partial interaction of α-Fe_2O_3MSs with biomolecules present in the *Myrtus cumini L.* leaf extract. This behavior is common in biogenically synthesized particles. While Figure 5d the micrograph PdNCs α-Fe_2O_3MSs showed deepening of ridges on the microsphere surface, more crystalline and PdNCs of various size distributions attached on its surface. The average particle size of green synthesized palladium nanoparticles were 15-250 nm and of cubical shape.
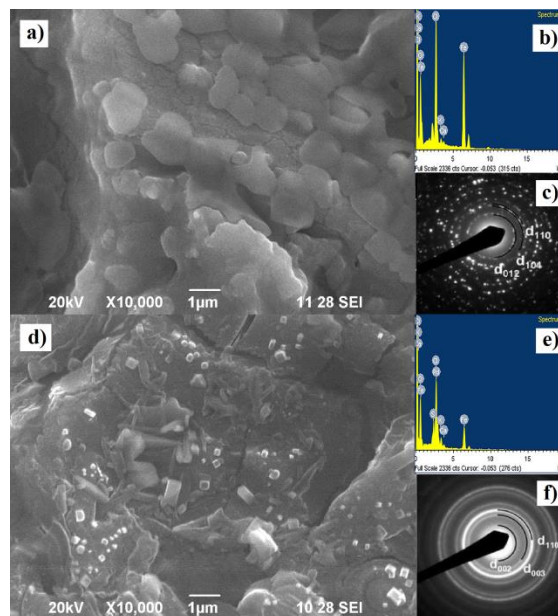
Figure 5. (a) α-Fe_2O_3 MSs SEM image (b) α-Fe_2O_3 MSs EDS spectrum (c) α-Fe_2O_3 MSs SADE pattern (d) PdNCs α-Fe_2O_3 MSs SEM image (e) PdNCs α-Fe_2O_3 MSs EDS spectrum (f) PdNCs α-Fe_2O_3 MSs SADE pattern

Figure 5b and e illustrate the EDS spectra of α-Fe$_2$O$_3$MSs and PdNCs embedded α-Fe$_2$O$_3$MSs. The observed peaks at 6.38, 3.28, 3.66,0.52 and 2.62 keV corresponds to the spectral lines of Fe-K$_\alpha$, K-K$_\alpha$, Ca-K$_\alpha$, O-K$_\alpha$ and Cl-K$_\alpha$ respectively, confirming the presence of Fe, O and trace amount of impurities like K, Ca and Cl in the α-Fe$_2$O$_3$MSs. Also the peaks at 2.90, 6.36, 2.28, 3.28, 3.66, 0.52 and 2.62 keV corresponds to the spectral lines of Pd-L$_\alpha$, Fe-K$_\alpha$,

S-K$_\alpha$, K-K$_\alpha$,Ca-K$_\alpha$, O-K$_\alpha$ and Cl-K$_\alpha$ respectively, confirming the presence of Pd, Fe, O and trace amount of impurities like S, K, Ca and Cl in the PdNCs embedded α-Fe$_2$O$_3$MSs. Figure 5c and f show the SADE pattern of α-Fe$_2$O$_3$MSs and PdNCs embedded α-Fe$_2$O$_3$MSs. The atomic percentage of elements present in α-Fe$_2$O$_3$MSs and PdNCs embedded α-Fe$_2$O$_3$MSs has been given in the Table 4.

Table 4. Elemental Composition of α-Fe$_2$O$_3$ MSs and PdNCs embedded α-Fe$_2$O$_3$ MSs

Samples	Elements	Atomic %
α-Fe$_2$O$_3$MSs	O K	65.09
	Cl K	15.27
	K K	0.76
	Ca K	0.33
	Fe K	18.55
	Total	100
PdNCs embedded α-Fe$_2$O$_3$MSs	O K	77.52
	S K	2.63
	Cl K	9.78
	K K	1.48
	Ca K	0.24
	Fe K	5.17
	Pd L	3.18
	Total	100

4.6. Box-Behnken analysis on decolorization of MO by UV-Fenten reaction

The optimization of decolorization of MO using α-Fe$_2$O$_3$MSs and PdNCs embedded α-Fe$_2$O$_3$MSs as photo catalyst BBD was done with three process parameters (pH, catalyst dosage and irradiation time) at three levels (-1, 0, +1). The experiments were performed for the

12 runs and 5 central points of the BBD, totally 17 runs rather than 27 runs in case of full factorial and results were fed to obtain a mathematical model. The predicted values were obtained by a model fitting technique using Design Expert 8.0.7.1 software and the values were shown in Table 5.

Table 5. Box-Behnken experimental design matrix and its response

Run	pH	Catalyst Dosage (g/L)	Irradiation time (min)	α-Fe$_2$O$_3$ MSs			PdNCs embedded α-Fe$_2$O$_3$ MSs		
				Y_{exp}	Y_{pre}	Residual	Y_{exp}	Y_{pre}	Residual
1	2	5	90	83.1	82.68	-0.51	87.2	87.26	0.07
2	3	1	60	78.5	78.18	-0.41	88.5	88.17	-0.37
3	1	3	30	76.5	75.95	-0.72	89.6	89.37	-0.26
4	3	5	60	74.5	74.38	-0.17	83	82.70	-0.36
5[a]	2	3	60	91.8	92.22	0.46	96.4	95.88	-0.54
6	2	1	90	88.6	88.37	-0.26	92.67	92.77	0.10
7[a]	2	3	60	92.6	92.22	-0.41	95.3	95.88	0.60
8	1	5	60	77.33	77.65	0.41	86.4	86.73	0.38
9[a]	2	3	60	92.2	92.22	0.02	95.7	95.88	0.19
10	2	1	30	77.2	77.62	0.54	90.5	90.44	-0.07
11	3	3	30	78.6	78.50	-0.13	86.2	86.59	0.45
12	2	5	30	73.7	73.93	0.31	85.3	85.21	-0.11
13[a]	2	3	60	92	92.22	0.24	96.1	95.88	-0.23
14[a]	2	3	60	92.5	92.22	-0.30	95.9	95.88	-0.02
15	1	3	90	92.3	92.40	0.11	93.1	92.71	-0.42
16	3	3	90	81	81.55	0.67	87.4	87.63	0.27
17	1	1	60	83.1	83.23	0.15	91.7	92.00	0.32

[a]Denotes the central points

The adequacy of the model was checked by fitting the experimental data with four high degree polynomial models viz., linear, interactive (2FI), quadratic and cubic models over which sequential model sum of squares and model summary statistics tests were carried out. Model

summary indicated that the quadratic models were highly sufficient and suggested for the decolorization study with the p-value less than 0.0001 and higher sequential model sum of squares for both α-Fe$_2$O$_3$MSs (524.16) and PdNCs embedded α-Fe$_2$O$_3$MSs (200.94).

4.7. Fitting of second order polynomial equation and statistical analysis

The empirical correlation between the experimental results of decolorization of MO obtained on the basis of BBD model derived from Equation (6) and the input variables (pH-X_1, catalyst dosage-X_2, irradiation time-X_3) were expressed in terms of a second order polynomial equation in terms of the coded factors for the two catalysts were given as Equations (8) for decolorization % using α-Fe$_2$O$_3$ MSs and Equations (9) for decolorization % using PdNCs embedded α-Fe$_2$O$_3$ MSs.

$$Y_1 = 92.22 - 2.08X_1 - 2.35X_2 + 4.87X_3 + 0.44X_1X_2 - 3.35X_1X_3 \\ -0.5X_2X_3 - 6.21X_1^2 - 7.66X_2^2 - 3.91X_2^3 \tag{8}$$

$$Y_2 = 95.88 - 1.96X_1 - 2.68X_2 + 1.1X_3 + 0.05X_1X_2 - 0.57X_1X_3 - 0.067X_2X_3 \\ -4.16X_1^2 - 4.32X_2^2 - 2.64X_2^3 \tag{9}$$

The results from Table 7 indicated that the model equations involving the relationship between the process parameters (X_1, X_2, and X_3) and the responses (Y_1 and Y_2) were found adequate. The significance of each parameter was evaluated using analysis of variance (ANOVA) followed by Fisher's statistical test (F-test) and F-value for all linear, square and interactive variables in both the second order polynomial equations were determined. The F-value indicated the influence of each controlled factor on the tested model (Kapur *et al.*, 2016). The ANOVA results for photo catalysts α-Fe$_2$O$_3$ MSs and PdNCs embedded α-Fe$_2$O$_3$ MSs showed larger Fisher F-values of 371.29 and 153.58, which implied that the model was significant and there was less variation in the response. The associated p-values were lower than 0.0001 indicating the models were statistically significant (Greenland *et al.*, 2016). The ANOVA results for both photo catalysts α-Fe$_2$O$_3$ MSs and PdNCs embedded α-Fe$_2$O$_3$ MSs depicted that the model terms X_1, X_2, X_3, X_{13}, X_1^2, X_2^2 and X_3^2 had p-values less than 0.0001 and were significant.

The quadratic models were found to have high values of "Adjusted R-Squared" greater than 98 % and "Predicted R-Squared" greater than 95 % showing that there was a deviation less than 5 %. The lack of fit test indicated that the quadratic model was found to have the minimum F value and p-value thus having insignificant lack of fit. For the α-Fe$_2$O$_3$ MSs Y_1 model the "Lack of Fit F-value" of 3.90 denoted the Lack of Fit was not significant relative to the pure error and the p-value from this test suggests that there was 11.08 % chance of insignificance. Similarly for the PdNCs embedded α-Fe$_2$O$_3$ MSs Y_2 model the "Lack of Fit F-value" of 1.61 denoted the Lack of Fit was not significant relative to the pure error and the p-value from this test suggesting that there was 31.97 % chance of insignificance. But this large value might be due to noise. The non-significant lack of fit was good and the models were found to be fit (Azad *et al.*, 2015). A high coefficient of determination (R^2) ensured a satisfactory adjustment of the quadratic model to the experimental data. The adjusted R^2 value, which is the measure of fitness and adequacy of the model compares the model and corrects the R^2 value of the sample size with the number of predicted terms. The value of adjusted R^2 (0.9952 for α-Fe$_2$O$_3$ MSs and 0.9885 for PdNCs embedded α-Fe$_2$O$_3$) were also high for the models and justifies a high correlation between the observed (Y_{exp}) and the predicted values (Y_{pre}).

4.8. Effect of process parameters on decolorization of MO

Decolorization of MO was carried out at different process parameters such as pH, catalyst dosage and irradiation time with an objective of determining optimum conditions. RSM plots were used to represent the effect of process parameters on decolorization of MO with initial concentration of 20 mg L^{-1}, temperature 50 °C and H$_2$O$_2$ concentration of 29.07 mM. Figure 6 exhibits the influence of pH (X_1), catalyst dosage (X_2) and irradiation time (X_3) on decolorization of MO using α-Fe$_2$O$_3$ MSs photocatalyst, where the significance of interactive variables was given in terms of response surface plots. The variables such as pH, catalyst dosage and irradiation time were found to significantly affect the decolorization of MO with $p<0.0001$ individually. The interactive effect of two interactive variables X_1X_2 and X_2X_3 showed negative effect while X_1X_3 showed a positive effect with significance of $p<0.0001$. It was observed from the Figure 6a that the maximum decolorization was between the pH (1-3) and catalyst dosage (1-5 g L^{-1}), both the variables exhibiting quadratic effect. From Figure 6c the irradiation time (30-90 min) exhibited a linear effect on decolorization of MO while pH (1-3) had a quadratic effect. Irradiation time and decolorization of MO were linearly correlated, where with the increase in irradiation time from 30 to 90 min, decolorization % also significantly increased. With respect to catalyst dosage the maximum value was obtained in the range of 1-5 g L^{-1} as shown in Figure 6b and other parameters also had a major influence on catalytic effect or the catalyst activity. The decolorization of MO using PdNCs embedded α-Fe$_2$O$_3$ MSs photocatalyst revealed the same trend of response (Figure 6d, e and f), yet the effectiveness of the catalyst was observed to be more.
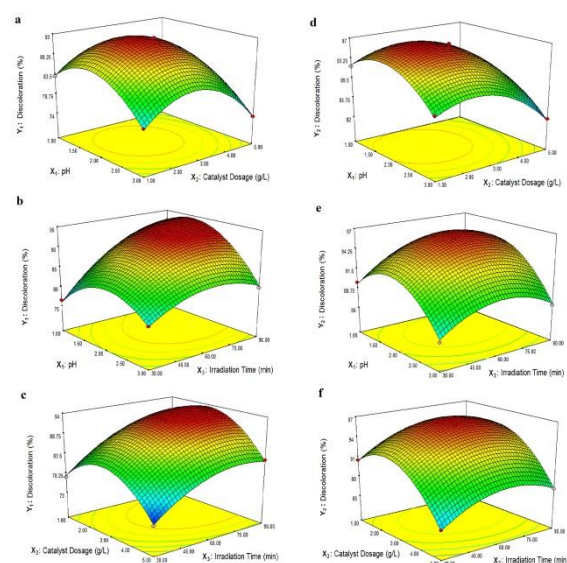
Figure 6. 3D response surface plots showing the effects of variables on the discoloration of MO using (a,b,c) α-Fe$_2$O$_3$MSs (d,e,f) PdNCs embedded α-Fe$_2$O$_3$MSs

4.9. Selection of optimum conditions

RSM optimization study for the decolorization of MO using α-Fe$_2$O$_3$MSs and PdNCs embedded α-Fe$_2$O$_3$MSs photocatalysts was performed to obtain maximum decolorization %. The Derringer's desirability function (D) was employed to optimize the process parameters for multiple responses. This function searches for a combination of process parameters: pH (X_1), catalyst dosage (X_2) and irradiation time (X_3) and jointly optimize both the responses Y_1 and Y_2 by satisfying the requirements for the maximum response in the design. In the present study, there was a single response variable i.e. discolorization % but obtained for two different catalysts. The optimization was accomplished by converting the responses Y_1 and Y_2 into a dimensionless desirability scale defining the partial desirability functions d_1 and d_2. Thereby combining these individual desirabilities d_1 and d_2 into a global desirability function, and maximizing it in the ranges between 0 (completely undesirable response) and 1 (fully desirable response) the optimal factor settings were identified (Balasubramani *et al.*, 2015).

The individual desirabilities d_1 and d_2 were obtained by choosing the goal, i.e. maximizing the decolorization % and specifying boundaries required for each variable. A weight factor of 1 was chosen for d_1 and d_2 here with default importance as 3 and this defines the shape of the desirability function. The process parameters were set at pH (1-3), catalyst dosage (1-5 g L^{-1}), irradiation time (30-90 min) and maximum for decolorization %. Applying the desirability function methodology for α-Fe$_2$O$_3$MSs and PdNCs embedded α-Fe$_2$O$_3$MSs, the optimum level of parameters obtained were pH 1.72, catalyst dosage 2.69 g L^{-1} and irradiation time 68.34 min for maximum decolorization of 93.85 and 96.56% respectively. Compared to the results obtained by using other Fenton catalysts like mesoporous Fe$_2$O$_3$–SiO$_2$ composite, α-Fe$_2$O$_3$-supported HY zeolite, Fe$_3$O$_4$/MWCNTs nanocomposites, Fe$_3$O$_4$ nanoparticles, steel industry waste for degradation of MO, PdNCs embedded α-Fe$_2$O$_3$MSs displayed a higher discoloration ratio even at a lower reaction time (Panda *et al.*, 2011; Jaafar *et al.*, 2012; Xu *et al.*, 2016; Zhao *et al.*, 2016; Ali *et al.*, 2013). Even though a higher amount of PdNCs embedded α-Fe$_2$O$_3$MSs catalyst dosage was used for decolorization, the main advantage was the lower reaction time, recoverability. Also no other harmful carcinogenic chemicals were used for catalyst synthesis.

5. Conclusion

Palladium embedded iron oxide particles were successfully synthesized using *Myrtus cumini* L. leaf extract as reducing agent. FT-IR analysis showed that *Myrtus cumini* L. leaf extract was rich in flavonoids and was proved to be an effective reducing agent. The crystallinity of the synthesized particles was analyzed using XRD and the catalyst was confirmed to have FCC Pd nanoparticles embedded on α-Fe$_2$O$_3$ microsphere matrix. The SEM/EDS analysis proved the presence of cubic Pd in the size range of 15-250 nm and the elemental composition of the microsphere surface. In this study,

Box-Behnken Design of statistical approach was applied effectively in finding the optimal process parameters for decolorization of MO by UV Fenton reaction by using both α-Fe$_2$O$_3$MSs and PdNCs embedded α-Fe$_2$O$_3$MSs as photocatalysts. The results indicated that the process conditions (pH; catalyst dosage, g L^{-1}; and irradiation time, min) had a significant effect on the decolorization of MO. The 3D response surface plots were employed to estimate the influence and interactive effect of process conditions on the response. The second order polynomial models Y_1 and Y_2 were derived for predicting effectiveness of the photocatalysts. The ANOVA indicated a high coefficient of determination (R^2) of 0.9979 for α-Fe$_2$O$_3$MSs and 0.995 for PdNCs embedded α-Fe$_2$O$_3$MSs ensuring a satisfactory fit with the experimental data. The process conditions for decolorization of MO using α-Fe$_2$O$_3$MSs and PdNCs embedded α-Fe$_2$O$_3$MSs were found to be optimum at pH 1.72, catalyst dosage 2.69 g L^{-1} and irradiation time 68.34 min that resulted in the maximum decolorization of 93.85 and 96.56 % respectively. These predicted process conditions agreed closely with the experimental values of decolorization % agreed closely and the models generated were found to be adequate. Thus PdNCs embedded α-Fe$_2$O$_3$MSs can be effectively used as Fenton catalyst. The statistical analysis of the experimental results confirmed that the trend of the Fenton catalytic activity of synthesized catalyst and the polynomial models generated can be used for similar studies in future.

References

Ali A., Hira Zafar M.Z., ul Haq I., Phull A.R., Ali J.S. and Hussain A. (2016), Synthesis, characterization, applications, and challenges of iron oxide nanoparticles, *Nanotechnology, Science and Applications*, **9**, 49.

Ali M.E., Gad-Allah T.A. and Badawy M.I. (2013), Heterogeneous Fenton process using steel industry wastes for methyl orange degradation, *Applied Water Science*, **3**, 263.

Ayyanar M. and SubashBabu P. (2012), Syzygium cumini (L.) Skeels: A review of its phytochemical constituents and traditional uses, *Asian Pacific Journal of Tropical Biomedicine*, **2**, 240.

Azad F.N., Ghaedi M., Dashtian K., Montazerozohori M., Hajati S. and Alipanahpour E. (2015), Preparation and characterization of MWCNTs functionalized by N-(3-nitrobenzylidene)-N'-trimethoxysilylpropyl-ethane-1, 2-diamine for the removal of aluminum(III) ions via complexation with eriochrome cyanine R: spectrophotometric detection and optimization, *RSC Advances*, **5**, 61060.

Balasubramani P., Palaniswamy P.T., Visvanathan R., Thirupathi V., Subbarayan A. and Maran J.P. (2015), Microencapsulation of garlic oleoresin using maltodextrin as wall material by spray drying technology, *International Journal of Biological Macromolecules*, **72**, 210.

Dias A.M., Hussain A., Marcos A.S. and Roque A.C. (2011), A biotechnological perspective on the application of iron oxide paramagnetic colloids modified with polysaccharides, *Biotechnology Advances*, **29**, 142.

Feng J., Hu X. and Yue P.L. (2004), Novel bentonite clay-based Fe-nanocomposite as a heterogeneous catalyst for photo-fenton discoloration and mineralization of orange II, *Environmental Science & Technology*, **38**, 269.

Ferreira S.C., Bruns R.E., Ferreira H.S., Matos G.D., David J.M., Brandao G.C., da Silva E.P., Portugal L.A., Dos Reis P.S., Souza A.S. and Dos Santos W.N.L. (2007), Box-Behnken design: an alternative for the optimization of analytical methods, *Analytica Chimica Acta*, **597**, 179.

Ghorbanloo M., Demirci S. and Sahiner N. (2015), PEI-M [M: Cu (II) and Co(II)] Hydrogel Catalyst For Methyl Orange Degradation And Epinephrine Oxidation, Çanakkale Onsekiz Mart Üniversitesi Fen Bilimleri Enstitüsü Dergisi; Cilt 1, Sayı **1**, 1.

Greenland S., Senn S.J., Rothman K.J., Carlin J.B., Poole C., Goodman S.N. and Altman D.G. (2016), Statistical tests, P values, confidence intervals, and power: a guide to misinterpretations, *European Journal of Epidemiology*, **31**, 337.

Harrell Jr F.E. (2015), Regression modeling strategies: with applications to linear models, logistic and ordinal regression, and survival analysis, Springer, 2nd ed., Heidelberg.

Jaafar N.F., Jalil A.A., Triwahyono S., Muhid M.N.M., Sapawe N., Satar M.A.H. and Asaari H. (2012), Photodecolorization of methyl orange over α-Fe_2O_3-supported HY catalysts: The effects of catalyst preparation and dealumination, *Chemical Engineering Journal*, **191**, 112.

Jamshaid T., Neto E.T., Eissa M.M., Zine N., Kunita M.H., El-Salhi A.E. and Elaissari A. (2016), Paramagnetic particles: From preparation to lab-on-a-chip, biosensors, microsystems and microfluidics applications, *TrAC, Trends in Analytical Chemistry*, **79**, 344.

Kanchana A., Devarajan S. and Ayyappan S.R. (2010), Green synthesis and characterization of palladium nanoparticles and its conjugates from Solanum trilobatum leaf extract, *Nano-Micro Letters*, **2**, 169.

Kapur M., Gupta R. and Mondal M.K. (2016), Parametric optimization of Cu(II) and Ni(II) adsorption onto coal dust and magnetized sawdust using box-behnken design of experiments, *Environmental Progress & Sustainable Energy*, **35**, 1597.

Khani H. and Wipf D.O. (2017), Iron Oxide Nanosheets and Pulse-Electrodeposited Ni–Co–S Nanoflake Arrays for High-Performance Charge Storage, *ACS Applied Materials & Interfaces*, **9**, 6967.

Khanna P.K., More P.V., Jawalkar J.P. and Bharate B.G. (2009), Effect of reducing agent on the synthesis of nickel nanoparticles, *Materials Letters*, **63**, 1384.

Kidambi S. and Bruening M.L. (2005), Multilayered polyelectrolyte films containing palladium nanoparticles: synthesis, characterization, and application in selective hydrogenation, *Chemistry of Materials*, **17**, 301.

Kubiak T.M. and Benbow D.W. (2009), The certified six sigma black belt handbook: Hypothesis Testing, ASQ Quality Press, Milwaukee, Wisconsin, pp. 230–264.

Kumar V., Yadav S.C. and Yadav S.K. (2010), Syzygium cumini leaf and seed extract mediated biosynthesis of silver nanoparticles and their characterization, *Journal of Applied Chemistry and Biotechnology*, **85**, 1301.

Kumar V. and Yadav S.K. (2012), Characterisation of gold nanoparticles synthesised by leaf and seed extract of Syzygium cumini L, *Journal of Experimental Nanoscience*, **7**, 440.

Logeswari P., Silambarasan S. and Abraham J. (2015), Synthesis of silver nanoparticles using plants extract and analysis of their antimicrobial property, *Journal of Saudi Chemical Society*, **19**, 311.

Ma Y., Huang Y., Cheng Y., Wang L. and Li X. (2014a), Biosynthesized ruthenium nanoparticles supported on carbon nanotubes as efficient catalysts for hydrogenation of benzene to cyclohexane: An eco-friendly and economical bioreduction method, *Applied Catalysis A: General*, **484**, 154.

Ma Y., Huang Y., Cheng Y., Wang L. and Li X. (2014b), Selective liquid-phase hydrogenation of maleic anhydride to succinic anhydride on biosynthesized Ru-based catalysts, *Catalysis Communications*, **57**, 40.

Mahdavi M., Namvar F., Ahmad M.B. and Mohamad R. (2013), Green biosynthesis and characterization of magnetic iron oxide (Fe_3O_4) nanoparticles using seaweed (Sargassum muticum) aqueous extract, *Molecules*, **18**, 5954.

Mallikarjuna K., Sushma N.J., Reddy B.S., Narasimha G. and Raju B.D. (2013), Palladium nanoparticles: single-step plant-mediated green chemical procedure using Piper betle leaves broth and their anti-fungal studies, *International Journal of Chemistry Analytical Science*, **4**, 14.

Maran J.P. and Manikandan S. (2012), Response surface modeling and optimization of process parameters for aqueous extraction of pigments from prickly pear (Opuntia ficus-indica) fruit, *Dyes and Pigments*, **95**, 465.

Maran J.P., Manikandan S., Priya B. and Gurumoorthi P. (2015), Box-Behnken design based multi-response analysis and optimization of supercritical carbon dioxide extraction of bioactive flavonoid compounds from tea (Camellia sinensis L.) leaves, *Journal of Food Science and Technology*, **52**, 92.

Molaie R., Farhadi K., Forough M. and Emamali R.S. (2012), Biological and green synthesis of palladium nanoparticles using aqueous extract of Pistacia atlantica plant's fruit: a facile biological approach. In Proceedings of the 4th International Conference on Nanostructures (ICNS4), 12–14 March, Kish Island I.R. Iran.

Nadagouda M.N. and Varma R.S. (2008a), Green synthesis of Ag and Pd nanospheres, nanowires, and nanorods using vitamin B_2: catalytic polymerisation of aniline and pyrrole, *Journal of Nanomaterials*, 3.

Nadagouda M.N. and Varma R.S. (2008b), Green synthesis of silver and palladium nanoparticles at room temperature using coffee and tea extract, *Green Chemistry*, **10**, 859.

Newman J.D. and Blanchard G.J. (2006), Formation of gold nanoparticles using amine reducing agents, *Langmuir*, **22**, 5882.

Nidheesh P.V. (2015), Heterogeneous Fenton catalysts for the abatement of organic pollutants from aqueous solution: a review, *RSC Advances*, **5**, 40552.

Panda N., Sahoo H. and Mohapatra S. (2011), Decolourization of methyl orange using Fenton-like mesoporous Fe_2O_3–SiO_2 composite, *Journal of Hazardous Materials*, **185**, 359.

Parveen K., Banse V. and Ledwani L. (2016), Green synthesis of nanoparticles: Their advantages and disadvantages, In Sharma N.N., Gaol F.L., Akhtar J., editors. AIP Conference Proceedings, **1724**, 020048.

Patel D., Moon J.Y., Chang Y., Kim T.J. and Lee G.H. (2008), Poly (D, L-lactide-co-glycolide) coated superparamagnetic iron oxide nanoparticles: Synthesis, characterization and in vivo study as MRI contrast agent, *Colloids and Surfaces A: Physicochemical and Engineering Aspects*, **313**, 91.

Petla R.K., Vivekanandhan S., Misra M., Mohanty A.K. and Satyanarayana N. (2012), Soybean (Glycine max) leaf extract based green synthesis of palladium nanoparticles, *Journal of Biomaterials and Nanobiotechnology* **3**, 14.

Prasad R. and Swamy V.S. (2013), Antibacterial activity of silver nanoparticles synthesized by bark extract of Syzygium cumini, *Journal of Nanoparticle*, **1**, 1.

Prasad R., Swamy V.S., Prasad K.S. and Varma A. (2012), Biogenic synthesis of silver nanoparticles from the leaf extract of Syzygium cumini (L.) and its antibacterial activity, *International Journal of Pharmaceutical and Biological Sciences*, **3**, 745.

Raheman F., Deshmukh S., Ingle A., Gade A. and Rai M. (2011), Silver nanoparticles: novel antimicrobial agent synthesized from an endophytic fungus Pestalotia sp. isolated from leaves of Syzygium cumini (L), *Nano Biomedicine and Engineering*, **3**, 174.

Rajendran S.P. and Sengodan K. (2017), Synthesis and characterization of zinc oxide and iron oxide nanoparticles using Sesbania grandiflora leaf extract as reducing agent, *Journal of Nanoscience*, **1**, 1.

Sachdev S., Maugi R., Kirk C., Zhou Z., Christie S.D. and Platt M. (2017), Synthesis and Assembly of Gold and Iron Oxide Particles within an Emulsion Droplet; Facile Production of Core@Shell Particles, *Colloid and Interface Science Communications*, **16**, 14.

Scheuermann G.M., Rumi L., Steurer P., Bannwarth W. and Mülhaupt R. (2009), Palladium nanoparticles on graphite oxide and its functionalized graphene derivatives as highly active catalysts for the Suzuki–Miyaura coupling reaction, *Journal of the American Chemical Society*, **131**, 8262.

Shahwan T., Sirriah S.A., Nairat M., Boyacı E., Eroğlu A.E., Scott T.B. and Hallam K.R. (2011), Green synthesis of iron nanoparticles and their application as a Fenton-like catalyst for the degradation of aqueous cationic and anionic dyes, *Chemical Engineering Journal,* **172**, 258.

Shu H.Y. and Huang C.R. (1995), Degradation of commercial azo dyes in water using ozonation and UV enhanced ozonation process, *Chemosphere*, **31**, 3813.

Soltani R.D., Rezaee A., Khataee A.R. and Safari M. (2014), Photocatalytic process by immobilized carbon black/ZnO nano composite for dye removal from aqueous medium: Optimization by response surface methodology, *Journal of Industrial and Engineering Chemistry*, **20**, 1861.

Sun T., Zhang Z., Xiao J., Chen C., Xiao F., Wang S. and Liu Y. (2013), Facile and green synthesis of palladium nanoparticles-graphene-carbon nanotube material with high catalytic activity, *Science Reports*, **3**, 2527.

Tanaka K., Padermpole K. and Hisanaga T. (2000), Photocatalytic degradation of commercial azo dyes, *Water Research*, **34**, 327.

Thirugnanasambandham K., Sivakumar V., Maran J.P. and Kandasamy S. (2014), Chitosan based grey wastewater treatment—A statistical design approach, *Carbohydrate Polymers*, **99**, 593.

Ugalde-Saldivar V.M. (2011), Aerobic synthesis of palladium nanoparticles, *Reviews on Advanced Materials Science*, **27**, 31.

URL: http://www.iucngisd.org/gisd/species.php?sc=505 (22.07. 2018).

Wakelyn P.J. (2007), Health and safety issues in cotton production and processing, In Cotton. Woodhead Publishing, 460.

Wang B., Xu M., Chi C., Wang C. and Meng D. (2017), Degradation of methyl orange using dielectric barrier discharge water falling film reactor, *Journal of Advanced Oxidation Technologies*, **20**.

Wang L., Kumeria T., Santos A., Forward P., Lambert M.F. and Losic D. (2016), Iron Oxide Nanowires from Bacteria Biofilm as an Efficient Visible-Light Paramagnetic Photocatalyst, *ACS Applied Materials & Interfaces*, **8**, 20110.

Wang L.Y., Cai L.J., Shen D., Feng Y.G., Chen M. and Qian D.J. (2010), Reducing agents and capping agents in the preparation of metal nanoparticles, *Progress in Chemistry (Beijing, China)*, **22**, 580.

Xu H.Y., Shi T.N., Zhao H., Jin L.G., Wang F.C., Wang C.Y. and Qi S.Y. (2016), Heterogeneous Fenton-like discoloration of methyl orange using Fe_3O_4/MWCNTs as catalyst: process optimization by response surface methodology, *Frontiers of Materials Science*, **10**, 45.

Yiping L., Hadjipanayis G.C., Sorensen C.M. and Klabunde K.J. (1994), Structural and magnetic properties of ultrafine Fe-Pd particles, *Journal of Applied Physics*, **75**, 5885.

Youssef N.A., Shaban S.A., Ibrahim F.A. and Mahmoud A.S. (2016), Degradation of methyl orange using Fenton catalytic reaction. *Egyptian Journal of Petroleum*, **25**, 317.

Zhan G., Huang J., Du M., Abdul-Rauf I., Ma Y. and Li Q. (2011), Green synthesis of Au–Pd bimetallic nanoparticles: single-step bioreduction method with plant extract, *Materials Letters*, **65**, 2989.

Zhang R., Xue M., Wang B., Ling L. and Fan M. (2019), C2H2 Selective Hydrogenation over the M@ Pd and M@ Cu (M = Au, Ag, Cu and Pd) Core-Shell Nanocluster Catalysts: The Effects of Composition and Nanocluster Size on Catalytic Activity and Selectivity, *The Journal of Physical Chemistry C* **123**, 16107.

Zhao H., Weng L., Cui W.W., Zhang X.R., Xu H.Y. and Liu L.Z. (2016), In situ anchor of magnetic Fe_3O_4 nanoparticles onto natural maifanite as efficient heterogeneous Fenton-like catalyst, *Frontiers of Materials Science*, **10**, 300.

Zhou X., Yang H., Wang C., Mao X., Wang Y., Yang Y. and Liu G. (2010), Visible light induced photocatalytic degradation of rhodamine B on one-dimensional iron oxide particles, *The Journal of Physical Chemistry C*, **114**, 17051.